



PAPER

Electromechanical coupling in polaronic ceria





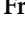




OPEN ACCESS

RECEIVED
4 December 2024REVISED
15 March 2025ACCEPTED FOR PUBLICATION
27 March 2025PUBLISHED
7 April 2025

Original content from this work may be used under the terms of the [Creative Commons Attribution 4.0 licence](#).

Any further distribution of this work must maintain attribution to the author(s) and the title of the work, journal citation and DOI.



Victor Buratto Tinti^{1,*} , Milica Vasiljevic¹ , Mathias Grønberg² , Huaiyu Chen³ ,
Valdemar Frederiksen² , Innokenty Kantor^{2,4} , Jesper Wallentin³ , Henrik Bruus² 
and Vincenzo Esposito^{1,*} 

¹ Department of Energy Conversion and Storage, Technical University of Denmark, B310, 2800 Kongens Lyngby, Denmark

² Department of Physics, Technical University of Denmark, B309, 2800 Kongens Lyngby, Denmark

³ Synchrotron Radiation Research and NanoLund, Lund University, Box 118, Lund 22100, Sweden

⁴ MAX IV Laboratory, Lund University, BOX 118, Lund 21100, Sweden

* Authors to whom any correspondence should be addressed.

E-mail: victin@dtu.dk and vies@dtu.dk

Keywords: ceria, electrostriction, thin film, polaron, impedance, nanostructure, defect chemistry

Supplementary material for this article is available [online](#)

Abstract

Oxygen-defective metal oxides like cerium oxides exhibit giant electrostriction and field-induced piezoelectricity due to a dynamic electrosteric interplay between oxygen defects, V_{O} , and the fluorite lattice. While such mechanisms are generally attributed to oxygen vacancies, recent results also highlight that trapped cationic defects, Ce'_{Ce} , i.e. small polarons, can contribute to the electromechanical properties of ceria. Here, we study nanocrystalline 5% Ca- and 10% Gd-doped ceria thin films with a high density of point defects and a constant oxygen vacancy concentration at 5% molar. We deposit thin films at low temperatures to promote microstructure disorder, i.e. nano-crystallinity, where the oxygen vacancies have low mobility due to high grain boundary interface densities. Still, the Ca^{2+} and Gd^{3+} dopants' sizes and valence differences modulate trapping effects toward the defects in the lattice, giving an insight into the electromechanical nature of the defects in the material dominating the electrostriction. We find that electrosteric dopant-oxygen vacancy interactions only slightly affect the electromechanical properties, which mainly depend on the frequency and intensity of the applied electric field. On the other hand, *n-type* polaron, Ce'_{Ce} , transport can emerge below the breakdown limit. These effects lead to an electromechanical coupling with a longitudinal electrostriction coefficient, M_{33} , above $10^{-16} \text{ V}^2 \text{ m}^{-2}$. Our results suggest that polaronic mechanisms substantially contribute to the electromechanical coupling in ceria. Also, the large ionic radius difference between Ce^{3+} and Ce^{4+} induces a large electro-strain upon polaron hopping, coupling electric stimuli to the observed electrostriction. This analysis provides new insights into the electromechanical effect of small polaronic semiconductive materials, opening new designing criteria for efficient electromechanical energy conversion.

1. Introduction

Electrostriction is a property exhibited by all insulating materials, characterized by a second-order coupling between electrical polarization and electrostrain [1]. Despite its ubiquity, electrostriction is less studied due to its typically lower electromechanical performance than piezoelectric materials, with the most commonly investigated electrostrictors being relaxors-ferroelectrics [2]. The electrostrictive coefficient, which describes the coupling between the squared electric field and the resulting strain, is typically denoted as M_{ij} . Newnham *et al* [3] established that the electromechanical properties of most materials follow an empirical relationship (1), linking the observed M_e to the material's compliance (s) and the dielectric permittivity ($\epsilon_0 \cdot \epsilon_r$) [4]. Recently, it was discovered that defective oxides can exhibit 'giant' electrostriction stemming from distinct electromechanical coupling mechanisms [4, 5]. Among the materials investigated, doped cerium oxide

ceramics have demonstrated exceptional performance [6],

$$M_e \approx 10^4 \cdot (s \cdot \epsilon_0 \cdot \epsilon_r)^{1.14}. \quad (1)$$

At first glance, ceria lacks the characteristics typically associated with high electromechanical performance. It exhibits a relatively low dielectric constant ($\epsilon_r \sim 30$) [7], a high elastic modulus (~ 200 GPa) [8], and a centrosymmetric crystalline structure (Fm $\bar{3}$ m) [9]. Nonetheless, under an applied external electric field, ceria-based ceramics show an electrostriction coefficient (M_e) ranging from 10^{-16} to 10^{-18} m² V⁻² [10–12], exceeding predictions based on Newnham's empirical relation by over two orders of magnitude [1, 4]. Moreover, ceria also shows high bias-induced effective piezoelectricity [4], i.e. *pseudo*-piezoelectricity [13], as thin films and bulk ceramics [7, 14]. Despite the relevant properties, the giant electromechanical coupling mechanisms remain under investigation.

Currently, the most widely accepted mechanism attributes giant electrostriction in ceria to its unique defect chemistry [6, 15]. Introducing point defects, such as oxygen vacancies ($V_{\text{O}}^{\cdot\cdot}$) and *n*-type polarons (Ce'_{Ce}), into the ceria lattice via thermo-chemical reduction or aliovalent doping induces anisotropic cell strain. Specifically, the bond length along the $V_{\text{O}}^{\cdot\cdot}$ axis ($\text{O}_{\text{O}}^{\times} - \text{Ce}'_{\text{Ce}} - V_{\text{O}}^{\cdot\cdot}$) expands, while orthogonal bonds ($\text{O}_{\text{O}}^{\times} - \text{Ce}'_{\text{Ce}} - \text{O}_{\text{O}}^{\times}$) contract, creating a local electro-elastic dipole [16]. Such distortion induces a symmetry change from fluorite to double-fluorite or intermediate states, depending on the defect chemistry and concentration. When an external electric field is applied, the $\text{O}_{\text{O}}^{\times} - \text{Ce}'_{\text{Ce}} - V_{\text{O}}^{\cdot\cdot}$ dipoles can be distorted and reoriented, enhancing the electromechanical coupling in oxygen-deficient materials [17]. Interestingly, rather than causing further unit cell distortion, the active sites and overall crystal structure tend to revert to a higher-symmetry configuration under an external electric field [16]. This symmetry transformation is primarily responsible for the anomalously high electrostriction observed, while the slow $V_{\text{O}}^{\cdot\cdot}$ kinetics accounts for the low-frequency dependence of the response [6]. Experimental evidence supporting this model primarily includes changes in Ce bond lengths under prolonged electrical bias [5, 16, 18] and computational simulations [19].

While the $V_{\text{O}}^{\cdot\cdot}$ -driven mechanism has gained acceptance, recent findings show that exceptionally high electromechanical responses have also been observed in isovalent-doped ceria, such as zirconia-doped ceria, where extrinsic vacancies are not introduced [20]. Interestingly, the addition of $V_{\text{O}}^{\cdot\cdot}$ was found to affect the material's properties adversely [21]. Moreover, Santucci *et al* recently showed that Ce^{3+} defects at the ceria's cation site can be formed in epitaxial gadolinium-doped ceria (GdDC) thin films under *in-plane* compressive strain, leading to enhanced electromechanical properties [22]. These results suggest that the underlying mechanism of giant electrostriction involves alternative or multiple contributing factors, such as electronic defects and defects complexes.

The Ce^{3+} electronic defects in ceria (Ce'_{Ce}) are easily formed from the Ce^{4+} to Ce^{3+} reduction. They have a 2:1 molar ratio with respect to the oxygen vacancies (two Ce^{3+} for each oxygen vacancy formed and four for each oxygen molecule desorbed) [23]. Still, they are *n*-type small polarons *quasi*-particles formed when charges interact electrostatically with the lattice, causing a localized distortion that moves with the charge carrier. Notably, polarons in ceria are already correlated to large electro-chemo-mechanical effects such as high-temperature mixed ionic–electronic conductivity effects and chemical expansion [24]. These properties arise from the different valence and cation size between the Ce^{4+} ionic radius of 0.97 Å in the ceria's fluorite structure compared to the Ce^{3+} ionic radius of 1.14 Å in the cubic coordination, i.e. in $\text{CeO}_{2-\delta}$, and 1.01 Å in the octahedral coordination, i.e. in Ce_2O_3 [25].

In this study, we aim to investigate further the role of defect chemistry and the impact of both extrinsic and intrinsic defects on the electromechanical response of defective ceria. We especially examined disordered thin films, i.e. nanocrystalline, of GdDC- and calcium-doped ceria (CaDC). Previous studies have shown that these compositions exhibit markedly different electromechanical behavior [15]. CaDC displays a frequency-independent response, whereas GdDC induces a non-Debye relaxation at low frequencies [7, 10]. These effects are attributed to the different dipole configurations in the lattices due to the sizes (Ca^{2+} : 1.12 Å and Gd^{3+} : 1.053 Å) and valences of the dopants [26] rather than a change in their concentration [12, 27].

We also compare the electrostriction behavior of GdDC and CaDC at specific doping levels of 10% (at.) and 5% (at.), respectively. These compositions were chosen based on prior research indicating that oxygen vacancies play a crucial role in their electromechanical coupling [12]. To ensure consistent extrinsic oxygen vacancy concentrations between the two samples, we selected half the calcium concentration compared to gadolinium due to the different valences of the dopants (Ca^{2+} and Gd^{3+}). Additionally, these doping levels are known to yield optimal performance for both Ca and Gd [10, 12].

Additionally, due to the nanocrystalline nature of the films, active polarization mechanisms may arise from frozen vacancy mobility at grain boundaries and interfaces. These disordered regions induce space-charge and charge carrier polarization, which are controlled by doping and defect configuration. This

effect significantly influences ionic mobility and vacancy configurations, ultimately altering the electrochemical response in the films [7].

2. Materials and methods

2.1. Thin film deposition

Thin films of 10% (at.) GdDC (10GdDC) and 5% (at.) CaDC (5CaDC) were deposited on 147 μm thick borosilicate glass substrates. The deposition was performed using magnetron sputtering, coupled with an RF power supply operating at 75 W and a self-bias voltage of ≈ 300 V. The depositions were carried out at room temperature (no substrate heating) for 1.5–3 h under an argon (99.999%) atmosphere (25 sccm, 5×10^{-2} mbar) with a 60 mm target-to-substrate distance, resulting in thin films with thicknesses ranging from 275 nm to 500 nm (figure S1). The thin films' compositions were achieved by employing different cerium oxide targets, being doped with 10% (at.) of Gd (*Kurt Lesker*, 99.99%) and 5% (at.) of Ca (*Testbourne*, 99.9%) for the 10GdDC and 5CaDC, respectively. The different doping ratios of 10% (at.) for Gd and 5% (at.) for Ca were chosen to maintain a constant nominal extrinsic oxygen vacancy concentration (5%) due to the different valence of the dopants.

Titanium nitride (TiN) was used as the electrode material due to its proven effectiveness in managing mechanical stress and electric fields for ceria-based actuators [28]. TiN electrodes were deposited via DC sputtering using TiN targets (*EvoChem*, 99.5%) at 50 W under 5.5×10^{-3} mbar pressure with 15 sccm of argon (99.999%) for 15 min, yielding electrode layers 100–150 nm thick. The devices were fabricated with a cross-plane geometry, where the ceria layer separated the top and bottom TiN electrodes. Mechanical shadow masks were used for electrode patterning.

2.2. Crystallographic and morphological characterization

The crystallographic properties of the films were analyzed using x-ray diffraction (XRD) with a *Panalytical Aeris* diffractometer in Bragg–Brentano geometry. Diffraction patterns were recorded over a 2θ range of 20° to 110° with a 0.01° step and a 20 s exposure per step. Measurements utilized $\text{CuK}\alpha$ radiation ($\lambda = 1.54 \text{ \AA}$) filtered by a nickel foil.

Raman spectroscopy measurements were performed using a *Renishaw InVia Reflex Confocal Raman* Microscope in backscattering geometry. A 532 nm laser was focused onto the samples through a 20x objective, resulting in a laser spot size of approximately 1 μm . Five Raman spectra were acquired from the samples, with a 10 s acquisition time for each spectrum. All measurements were conducted at room temperature under ambient conditions.

The morphology of the samples was characterized by using scanning electron microscopy (SEM) with a *Zeiss Ultra* microscope equipped with a field-emission gun. SEM was employed to analyze the microstructure, morphology, and film thickness. To visualize the cross-section of the samples, a sacrificial sample was fractured and coated with a 10 nm layer of carbon to minimize charging.

2.3. In situ synchrotron experiments

In situ XRD (*i*-XRD) experiments were conducted at the DanMAX beamline of the MAX IV synchrotron facility [29] (SI, S3). Samples were oriented in both reflection and transmission geometries relative to the incident x-ray beam. For *in situ* experiments, an external DC power supply applied stepwise voltages from 0 to 15 V at a rate of 10 mV s^{-1} . Electrical connections to the top and bottom electrodes were established using 25 μm copper wires bonded with conductive carbon paste. The x-ray energy was set to 15 keV, and diffraction patterns were collected with a *DECTRIS PILATUS3 X 2M CdTe* area detector. Diffraction patterns were captured every 1 s with a 0.1 s exposure time to minimize beam damage artifacts.

2.4. Electromechanical experimental setup

Electromechanical characterization was performed using a custom-built system at DTU [28]. Samples were mounted in a cantilever geometry, and displacements were measured at the cantilever's tip, following a previously reported laser-beam configuration [14]. Both alternating voltage and DC bias were applied using an *Aim-TTi* signal generator, with electrical connections established using 25 μm copper wires. Displacement measurements were conducted with a single-beam laser interferometer (*SIOS*), and the signals were processed using a lock-in amplifier (*Ametek Model 7230 DSP*). Each data point was recorded over a 120 s interval with a 0.1 s sampling rate, and the final displacement values were calculated as the average of the measured data [30]. It should be noted that we cannot experimentally differentiate between positive or negative displacements due to the use of a lock-in amplifier.

2.5. Modeling of electromechanical coupling mechanisms

The theoretical treatment builds on our previous work on piezoelectric actuation of microfluidic systems [14, 31, 32]. The independent fields are the mechanical displacement field \mathbf{u} and the electric potential ϕ . The dependent fields are the strain tensor $s = \frac{1}{2} [\nabla \mathbf{u} + (\nabla \mathbf{u})^T]$, the electric field $\mathbf{E} = -\nabla \phi$, as well as the stress tensor σ and the electric displacement D given by the constitutive equations (using index notation) for isotropic electrostrictive materials [14, 33]:

$$\sigma_{ij} = C_{ijkl}(Y, \nu) s_{kl} + m_{ijkl}(Y, \nu, M_{31}, M_{33}) E_k E_l + \varepsilon_{ik}^s \left(E_k E_j - \frac{1}{2} E_l E_l \delta_{ij} \right), \quad (2a)$$

$$D_i = -2 m_{ijkl}(Y, \nu, M_{31}, M_{33}) s_{kl} E_j + \varepsilon_{ij}^s E_j, \text{ with } i, j, k, l \text{ being } x, y, \text{ or } z. \quad (2b)$$

Here, Y is Young's modulus, ν is Poisson's ratio, M_{31} and M_{33} are respectively the shear and longitudinal electrostriction coefficients, ε_{ij}^s the electric permittivity (figures S2 and S3), δ_{ij} is the Kronecker delta, and the elastic moduli C_{ijkl} as well as the electromechanical coupling coefficients are given in terms of, ν , M_{31} , and M_{33} as described in the supplemental material (SI, S2). Note that we have extended the stress tensor from our previous work [14] by including the purely electric stress in the form of Maxwell's stress tensor [33], the last term on the right-hand side of equation (2). The governing equation (3) for \mathbf{u} (4a) and ϕ (4b) are,

$$\text{the Cauchy equ.: } \rho \partial_t^2 \mathbf{u} = \nabla \cdot \boldsymbol{\sigma}, \quad \text{the zero - free - charge Gauss equ.: } 0 = \nabla \cdot \mathbf{D}. \quad (3)$$

In the experimental setup, a driving voltage $V = V^{\text{DC}} + V^{\text{AC}} e^{i\omega t}$ consisting of a large DC component and a small AC component, $|V^{\text{AC}}| \ll |V^{\text{DC}}|$, is applied to the electrodes of the electrostrictor so that the electrostriction response to the leading order takes the form,

$$u_i = u_i^{(0)} + u_i^{(1)} e^{-i\omega t} + u_i^{(1)*} e^{i\omega t}, \quad (4a)$$

$$\phi = \phi^{(0)} + \phi^{(1)} e^{-i\omega t} + \phi^{(1)*} e^{i\omega t}, \quad (4b)$$

where the asterisk denotes complex conjugation. As in our previous work [14], we implement these equations in the Weak Form PDE Interface of Comsol Multiphysics, including only terms up to the first order in the response.

The material's properties and geometrical parameters used for the simulations can be found in table S1 and figure S4 [10, 14, 34–36].

2.6. Electrochemical impedance spectroscopy (EIS)

Electrical measurements were performed using a Solartron 1260A impedance analyzer. For electrical characterization, samples were deposited onto circular substrates (\varnothing 15 mm) under the same conditions as the cantilevers. Measurements were conducted in a Linkam sample holder, which allowed precise control of temperature and atmosphere, with the samples maintained under a constant argon flow. Electrical contacts were established using micromanipulators equipped with tungsten tips. EIS measurements were carried out over a frequency range of 1 MHz–10 mHz with a 5 mV alternating field. Bias (DC voltage) was also applied with the AC using the same setup. The impedance data was analyzed and fitted to an equivalent RC circuit model using ZView software.

3. Results and discussion

3.1. Electromechanical coupling

Figure 1(a) illustrates the crystallographic and morphological features of the doped ceria films. Highly defective thin films result from room temperature RF sputtering deposition on glass substrates. In such conditions, the microstructure is disordered, i.e. nanocrystalline, with a high-density grain boundary, including nonstoichiometric oxygen defect, likely frozen at the grain boundary [37]. Thin films of 5CaDC and 10GdDC were deposited with thicknesses ranging from 275 nm to 500 nm (figure S1). All samples show diffraction patterns compatible with the fluorite structure of ceria ($\text{Fm}\bar{3}\text{m}$) [9], with no additional phases visible.

For electromechanical characterization, the samples were coated with *out-of-plane* electrodes, forming a structure where the active ceria layer was sandwiched between top and bottom electrodes. The samples were then positioned in a cantilever geometry (see supplemental material, table S1 and figure S4), allowing actuation under high electric fields ($\approx 100 \text{ kV cm}^{-1}$) at low voltages ($< 10 \text{ V}$). The measurements were conducted under an applied bias to linearize the second-order electrostrictive response, resembling the inverse piezoelectric effect, often called the pseudo- or effective piezoelectric effect [4, 13].

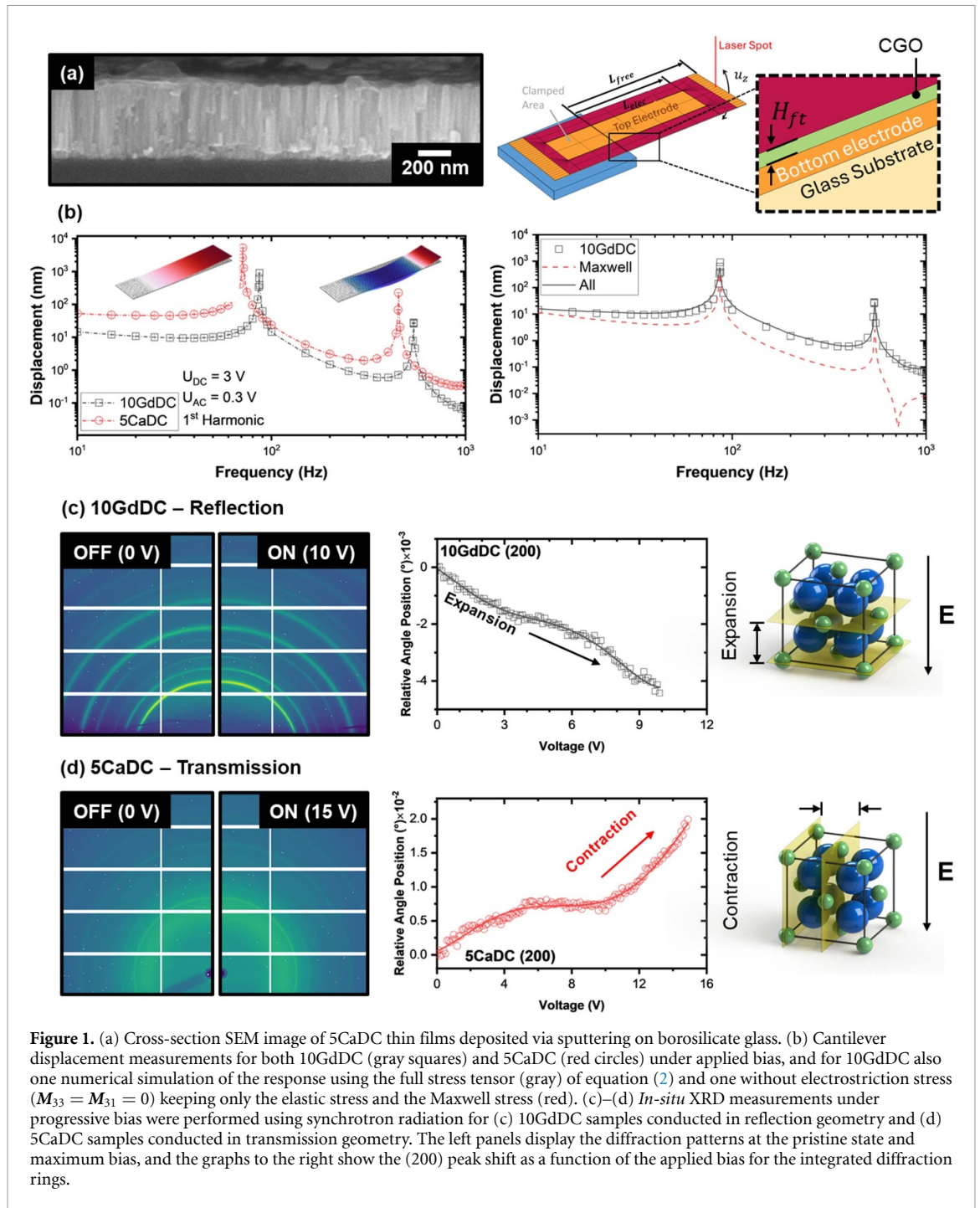


Figure 1(b) presents the electromechanical responses of 10GdDC and 5CaDC, measured in a cantilever configuration. Both first- and second-order resonant modes [38] are present, with minor variations attributed to differences in geometric factors such as clamping distances and electrode placement. Interestingly, the samples exhibit similar frequency-dependent responses regardless of the dopant. This contrasts with previous studies on bulk ceramics, where Ca- and Gd-doped ceria compositions exhibited significantly different frequency-dependent behavior [7, 10, 39]. Gd-doped ceria typically shows low-frequency non-Debye relaxation [40], while Ca-doped compositions exhibit frequency-independent responses [7, 10]. These differences were previously linked to dopant-defect interactions, specifically cation-defect association, which inhibits active sites with lower relaxation frequencies [7, 41]. The observed similarity between the samples in this study suggests that another mechanism, beyond dopant-defect interactions, dominates the electrostrictive coupling in the highly defective films.

Based on the model in section 2.5, we conducted numerical simulations to understand the electromechanical coupling responsible for the cantilever motion (figures 1(c) and S5). A detailed account of

Table 1. Relative comparison of low frequency (<10 Hz) electrostriction coefficient for the values found by numerical simulations of the experimental results in this work with previously reported results for similar compositions.

References	10GDDC		5CaDC	
	$ M_{33} $ ($\text{m}^2 \cdot \text{V}^{-2}$)	$ M_{31} $ ($\text{m}^2 \cdot \text{V}^{-2}$)	$ M_{33} $ ($\text{m}^2 \cdot \text{V}^{-2}$)	$ M_{31} $ ($\text{m}^2 \cdot \text{V}^{-2}$)
This work	$5.3 \cdot 10^{-16}$	$6.6 \cdot 10^{-21}$		$2.3 \cdot 10^{-19}$
[7]	$2.9 \cdot 10^{-17}$		$4.6 \cdot 10^{-18}$	
[10]			$1-3 \cdot 10^{-18}$	
[11]	$8.4 \cdot 10^{-17}$			
[12]	$8 \cdot 10^{-17}$			
[14]	$1.1 \cdot 10^{-16}$	$1.1 \cdot 10^{-19}$		
[16]	$1.6 \cdot 10^{-17}$			
[41]	$3 \cdot 10^{-17}$			
[44]		$0.4-9 \cdot 10^{-19}$		

the simulation results is given in the supplemental material (SI, S2), where in table S1 and figure S4, the geometry and parameter values used in the numerical simulation of the experiments are defined.

At low frequencies ($f < 10$ Hz), we found nearly constant values for the electrostriction coefficients M_{31} and M_{33} for both compositions. For 10GdDC, $M_{31} = 6.6 \times 10^{-21} \text{ m}^2 \cdot \text{V}^{-2}$ and $M_{33} = -5.3 \times 10^{-16} \text{ m}^2 \cdot \text{V}^{-2}$, with M_{31} being five orders of magnitude smaller than M_{33} . In contrast, for 5CaDC, $M_{31} = \pm 2.3 \times 10^{-19} \text{ m}^2 \cdot \text{V}^{-2}$, which is 50 times larger than in 10GdDC and sufficiently large to dominate the contribution from M_{33} . As a result, M_{33} cannot be determined in this case (figure S6). This notable difference in response between the two cantilevers arises because M_{31} acts over the unclamped electrode length (L_{elec}), whereas M_{33} acts only through fringe fields over the length defined by the films thickness (H_{tf}) [14].

The relative strengths of the shear and the longitudinal response are given by the ratio ($M_{31}L_{\text{elec}}/M_{33}H_{\text{tf}}$), which for 10GdDC is 0.76 and for 5CaDC is about 30, assuming the typical value $M_{33} = -3 \times 10^{-16} \text{ m}^2 \cdot \text{V}^{-2}$. Consequently, for 10GdDC, the overall response results from the elastic, the electrostrictive M_{31} - M_{33} stress, and the Maxwell stress, but for 5CaDC, it results mainly from the elastic, the electrostrictive M_{31} stress, and the Maxwell stress. The Maxwell stress tensor, often overlooked, plays a critical role in electromechanical behavior, especially when electrode separation is on the nanoscale, as in the *out-of-plane* configuration [42]. Furthermore, the results indicate that for ceria-based giant electrostrictors, M_{31} is several orders of magnitude smaller than M_{33} , often rendering it negligible depending on the geometry, a behavior atypical compared to traditional piezoceramic actuators [43].

The simulations (see details in SI, S1) also show that in 10GdDC, the Maxwell stress dominates over the electrostriction stress for $f < 10$ Hz, and that the electrostriction coefficients decrease weakly for $10 \text{ Hz} < f < 700 \text{ Hz}$, before they decay sharply for $700 \text{ Hz} < f < 5000 \text{ Hz}$, to become negligible for $f > 5000 \text{ Hz}$. (shown in figure S6). The observed decrease in the kHz regime aligns with previous findings for both thin films [14, 44] and bulk ceramics [7]. As a detail, we mention that for 10GdDC, the interplay between the three vibrational modes explains the absence of out-of-resonance minima in agreement with the experimental (figure S7). To illustrate the electromechanical performance observed for the doped-ceria films in this work, we compared our results to previous values reported in the literature in table 1.

To comprehend the electromechanical coupling mechanism in the samples at the structural level, we conducted *i*-XRD using monochromatic synchrotron radiation (figures 1(c) and (d)). Due to the short exposure time (0.1 s), we were able to continuously probe the crystallography during bias application while minimizing artifacts from prolonged bias and radiation exposure [45, 46]. No phase changes were observed upon applying an external electric field [45], with 10GdDC and 5CaDC remaining in the fluorite phase from zero to the maximum voltage of 15 V ($\approx 300 \text{ kV cm}^{-1}$). At first glance, no significant changes were apparent when comparing the pristine and biased samples. However, a closer analysis of peak diffraction shifts (figures S8 and S3) reveals a clear trend.

The *i*-XRD measurements reveal contrasting *in-plane* and *out-of-plane* strain responses for the ceria thin films. The 5CaDC sample, analyzed in a transmission geometry (figure 1(d)), primarily probes planes orthogonal to the applied electric field, allowing the detection of *in-plane* strain. The diffraction peak shift for 5CaDC reveals an isotropic contraction along the *in-plane* axes, with a negligible difference of approximately $5 \cdot 10^{-3}$ degrees between orthogonal positions, attributed to the signal-to-noise ratio (figure S9). A similar trend is also observed in diffraction patterns corresponding to the (111) and (311) planes (figure S8).

Conversely, the 10GdDC sample was measured in reflection geometry (figure 1(c)), which is primarily designed to probe *out-of-plane* strain but is also affected by *in-plane* features. At 90° (center of the diffraction arc), the measurement mainly reflects *out-of-plane* strain, while lateral angles, e.g. 30° , 45° , 135° , and 150° ,

include contributions from both *in-plane* and *out-of-plane* strains. The diffraction results, derived from the integrated arc, exhibit an overall shift corresponding to expansion (figure 1(c)). However, a detailed analysis at specific angles highlights an anisotropic strain distribution (figure S10).

Interestingly, a *built-in* anisotropy is observed in the pristine 10GdDC sample when comparing *in-plane* and *out-of-plane* planar distances. Although unexpected, similar anisotropy for polycrystalline thin films has been previously associated with electrochemical variations at the film–electrode interface [5, 47]. The peak shift at 90° exhibits a maximum expansion of 0.06% upon applying an electrical bias. In comparison, at 30°, it reduces to 0.015%, highlighting significant ovalization of the diffraction arc and confirming the anisotropic strain response.

Decomposing the strain into its *in-plane* and *out-of-plane* components for the 10GdDC sample reveals a distinct divergence in behavior. The *out-of-plane* strain shows a marked expansion trend, whereas the *in-plane* strain exhibits a smaller drift with a slight tendency toward contraction (figure S11), aligning with the *in-plane* contraction observed for 5CaDC. Although the *in-plane* contraction magnitude observed for the 10GdDC does not fully match that of the 5CaDC, the findings are consistent with the electromechanical findings. Specifically, the 10GdDC showed a weaker M_{31} coupling, while the 5CaDC showed a significantly stronger M_{31} component (figure S6).

Although 10GdDC and 5CaDC exhibit differences in their crystalline features, both samples show a similar overall structural response: expansion parallel to the field and contraction in the orthogonal directions. The reflection-mode *i*-XRD of 10GdDC captures both effects, while the transmission-mode *i*-XRD of 5CaDC confirms the orthogonal contraction, validating the overall behavior in both cases and indicating a common underlying electromechanical coupling mechanism. Based on extensive previous studies on ceria-based nanocrystalline films, the observed correlation between *in-plane* and *out-of-plane* responses in 10GdDC and 5CaDC is well-founded [46–50]. As shown in prior work, variations in doping composition may influence the magnitude or frequency dependence of the response but do not alter the fundamental electromechanical coupling in defective ceria [7, 11, 12].

These results indicate anisotropic strain in the unit cell relative to the applied electric field, ruling out isotropic effects such as thermal expansion due to Joule heating [51] or overall chemical reduction [52, 53]. The expansion and orthogonal contraction suggest M_{33} and M_{31} coupling and the correlation between lattice distortion and the giant electromechanical coupling in ceria [16]. This is the first report on the connection between parallel and orthogonal strain in the context of the electroactive properties of ceria. These findings are further supported by our previous study on similar materials deposited on flexible substrates [14].

However, not all observed strains can be solely attributed to electrostriction, as the magnitude would require electrostrictive coefficients exceeding those derived from the electromechanical characterization. Given that the *i*-XRD was conducted under increasing bias rather than an alternating field, other mechanisms that depend on slow kinetics, such as electrochemical interactions, could contribute to the observed strain, some of which may be irreversible. Nonetheless, the anisotropic strain response indicates a directional electromechanical coupling, reinforcing the link between lattice dynamics and the electroactive functionality of defective ceria. Further investigations are needed to fully elucidate all active mechanisms driving the observed *in-* and *out-of-plane* dynamics.

Three distinct regimes are apparent in both samples during the *i*-XRD (figures 1(c) and (d)). At lower biases (<5 V), the samples exhibit a near-linear trend, followed by saturation at intermediate values (5–9 V). Upon reaching a threshold voltage (>9 V), the peak drift accelerates with no further changes observed up to the maximum field. Saturation of electrostriction in ceria is well-documented [11, 40], particularly at low frequencies (<10 Hz), being particularly relevant to the quasi-static *i*-XRD measurements and may contribute to the initial drift followed by the plateau at intermediate biases. It has also been suggested that ceria polarization mechanisms under intense electric fields progress through three regimes: the polarization of carriers at grain boundaries and electrodes, followed by the formation of Schottky barriers and their subsequent collapse and charge injection at elevated fields due to electrochemical redox [45]. Furthermore, other effects, such as radiation-induced ionization of ceria, *i.e.* beam damage, cannot be entirely excluded due to the high intensity of the synchrotron source [54, 55].

3.2. Electrical polarization

We conducted EIS characterization to investigate the electromechanical responses of 5CaDC and 10GdDC (figure 2). Both samples exhibit interfacial polarization in their pristine state, forming an electrical double-layer at the ceria-electrode interface (figure 2(a)) for DC and *quasi*-DC electrical fields. While this is typical for ceria with blocking electrodes, TiN does not block electronic conduction. Instead, a TiO_x passivation layer likely formed during sputtering, and bias application appears to trigger an irreversible redox process, reducing the oxide layer and allowing charge carrier discharge at the interface.

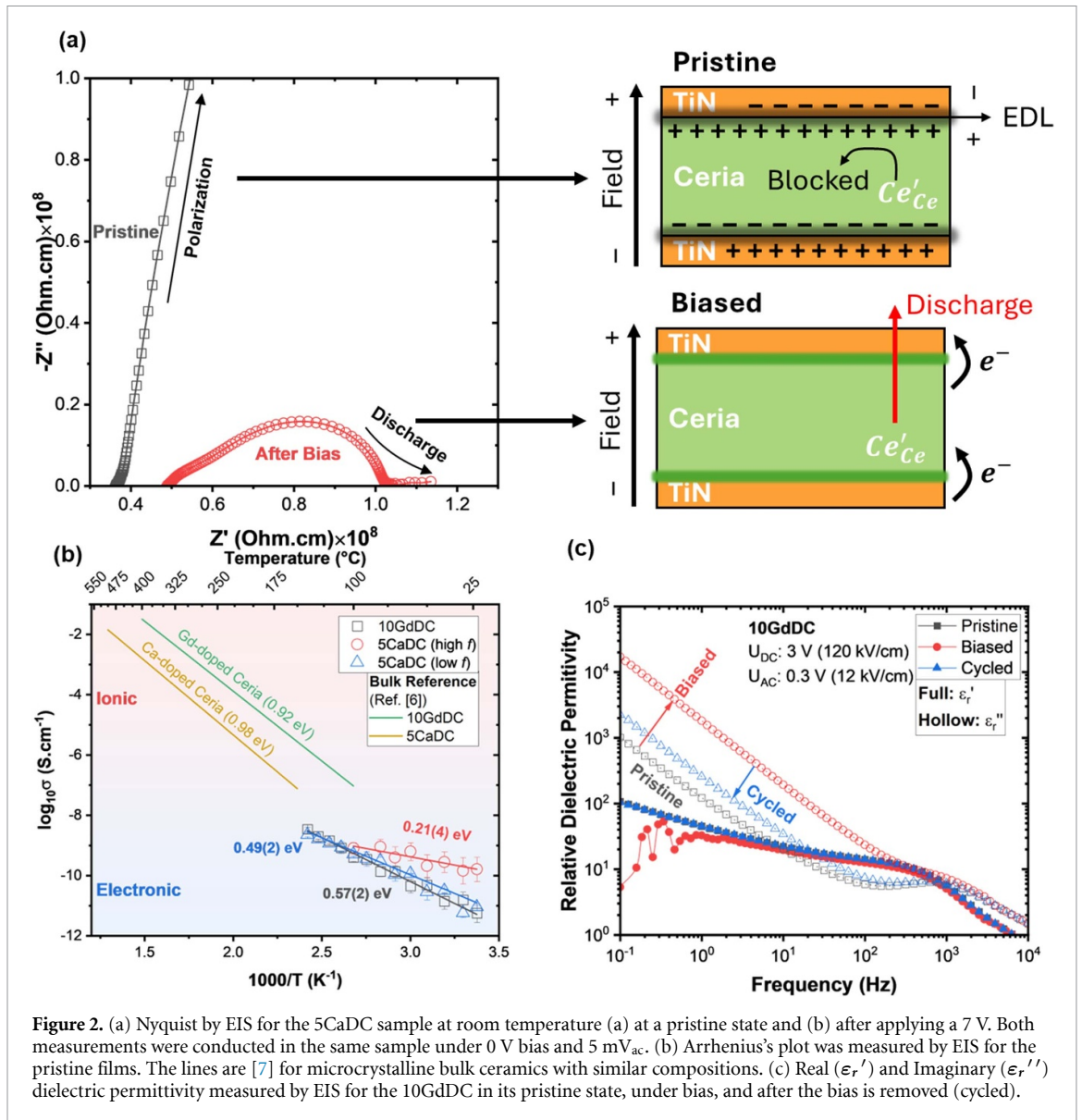


Figure 2. (a) Nyquist by EIS for the 5CaDC sample at room temperature (a) at a pristine state and (b) after applying a 7 V. Both measurements were conducted in the same sample under 0 V bias and 5 mV_{ac}. (b) Arrhenius's plot was measured by EIS for the pristine films. The lines are [7] for microcrystalline bulk ceramics with similar compositions. (c) Real (ϵ_r') and Imaginary (ϵ_r'') dielectric permittivity measured by EIS for the 10GdDC in its pristine state, under bias, and after the bias is removed (cycled).

After bias removal, a non-blocking interface remains, ruling out significant oxygen-ion conduction and pointing to *n-type* electronic conduction via polaron hopping [56, 57]. Temperature-dependent EIS (figure 2(b)) reveals activation energies between 0.49 and 0.57 eV, consistent with mixed ionic–electronic conduction, dominated by polaronic transport in nanocrystalline ceria [58, 59]. The estimated grain size (~ 10 nm, table S2) aligns with reports of enhanced electronic conduction in nanostructured ceria [60, 61]. Additionally, a high-frequency component in 5CaDC, with an activation energy of 0.21 eV, further suggests an electronic conduction mechanism.

Electrochemical changes are more pronounced in 5CaDC than in 10GdDC (figure 2(c)). While 10GdDC shows a modest conductivity increase, 5CaDC exhibits a dramatic enhancement by several orders of magnitude (figure 2(b)), with its polarization dominated by Maxwell–Wagner–Sillars behavior (figure S12) [62]. Upon bias removal, 5CaDC retains its low-resistance state (figure S13), suggesting a high density of mobile charge carriers and polaronic resistive switching. This aligns with the limited oxygen defect mobility at low temperatures (< 50 °C) [63] and the blocking effects introduced by nanocrystallinity [64]. The hysteretic behavior observed during heating and cooling (figures S14 and S15) further supports the strong electrochemical reactivity of these thin films, likely influenced by TiO₂ modifications at the interface.

Polaronic transport typically involves a conductive, non-volatile filament between electrodes, reducing resistivity [65]. However, filamentary switching typically occurs only in films thinner than 50 nm, making it unlikely in this work. Instead, the observed polaronic conduction was either intrinsic or induced by redox processes. Since 10GdDC and 5CaDC exhibit activation energies consistent with *n-type* conduction [24],

their pristine-state conductivity suggests further changes stemming from interfacial or electrochemical modifications.

The strong polaronic character and similar electromechanical responses of both samples suggest a correlation between these properties. In ceria, polaron hopping involves $\text{Ce}^{3+}/\text{Ce}^{4+}$ switching, inducing mechanical strain waves due to ionic radius differences (1.14 Å vs 0.97 Å) [26]. This effect couples electrical and mechanical responses independent of dopant type or concentration. While $\text{V}_{\text{O}}^{\bullet}$ contribute, Ce'_{Ce} defects may also drive electromechanical coupling, a mechanism often overlooked in favor of vacancy-centered models. Our results suggest that giant electromechanical coupling in ceria arises from both $\text{V}_{\text{O}}^{\bullet}$ reorganization and defect rearrangement at the cation site, aligning with recent studies on aliovalent doping [20, 21].

Despite their similar conductivities and activation energies (figure 2(b)), the bias-induced conductive switching is more easily observed in 5CaDC, while in the 10GdDC samples is less pronounced (figure S13). Such a difference may arise from 10GdDC's higher Gd content (10% vs 5% Ca), which could introduce electro-elastic barriers that hinder polaron formation. Additionally, stronger $\text{Ca}^{2+}-\text{V}_{\text{O}}^{\bullet}$ interactions might enhance clustering effects [66], further influencing switching behavior.

3.3. Structure and defect chemistry

We use XRD and Raman spectroscopy analysis to characterize further the chemical and structural typically associated with Ce'_{Ce} species (figure 3). XRD on the (111) peak shows a substantial shift due to a larger lattice in the materials (figure 3(a)). Such results confirm the *i*-XRD synchrotron data in figures 1(c) and (d), excluding the effect of beam damage. Aligning with SEM observations, the films exhibit broad peaks with multiple diffractions (figure S13), indicating nanometric grains and polycrystallinity. The average crystallite sizes were estimated by the Scherrer equation [67, 68] to be 9.6(25) nm and 7.7(29) nm for 10GdDC and 5CaDC, respectively. The grain sizes derived from XRD align with SEM observations, revealing nano-sized grains with a columnar microstructure characteristic of low-temperature sputtered ceria film deposition [13, 14, 44, 46, 69]. Both films exhibit unit cell parameters larger than the reference values calculated using Kim's expression [70], measured at 5.528(13) Å and 5.476(7) Å for 10GdDC and 5CaDC, respectively (table S2). Unit cell volume expansion is commonly reported for nanostructured ceramics and is linked to the higher fraction of grain boundaries and point defects [71]. The presence of nanograins in the sample can stabilize higher concentrations of Ce'_{Ce} , which induces lattice expansion due to the larger ionic radius of Ce^{3+} compared to the host Ce^{4+} [72].

Ceria exhibits an intrinsic Raman mode at 465 cm^{-1} ($\text{F}_{2\text{g}}$), which is associated with oxygen ionic vibrations around Ce^{4+} cations in the fluorite lattice [73] (figure 3(b)). For doped and defective materials, additional Raman modes are activated, with bands at 550 cm^{-1} ($\Delta 550$) and 600 cm^{-1} ($\Delta 600$) typically linked to point defects, such as dopant substitution, $\text{V}_{\text{O}}^{\bullet}$, and Ce'_{Ce} [6, 74].

The 10GdDC and 5CaDC samples show significantly more intense defect bands than previous reports on microcrystalline ceria [7], indicating a higher concentration of point defects. Notably, the 10GdDC sample exhibits a considerably more intense defect band than the 5CaDC (table S3), which aligns with the larger unit cell expansion observed in the XRD results. Additionally, the larger $\text{F}_{2\text{g}}$ drift for the 10GdDC to lower wavelengths indicates a lattice expansion, aligning with XRD results. While both 10GdDC and 5CaDC films are expected to have a higher concentration of defects due to their nanostructure and deposition under an oxygen-depleted atmosphere, the observed difference between the Ca- and Gd-doped films remains unclear. Whether this difference arises from dopant-defect interactions or from the different dopant concentrations used to maintain a constant nominal extrinsic oxygen deficiency (5%) is uncertain.

In summary, XRD and Raman spectroscopy results point to nanocrystalline films with point defect concentration exceeding the nominal predicted by the corresponding aliovalent doping for 10GdDC and 5CaDC. These results particularly indicate an oxygen-deficient system with high Ce'_{Ce} point defect concentration. This observation reinforces the polaronic-dominated electrical properties observed in figure 2.

3.4. Electro-chemo-mechanical coupling

We further probe the electro-chemo-mechanical coupling in the 10GdDC thin films by characterizing their dielectric properties in both pristine and biased states, as shown in figure 4. Upon applying bias, the imaginary relative dielectric permittivity (ϵ''_r) sharply increases and maintains an approximately constant value, even under bias reversal. This behavior indicates an enhancement in charge carrier mobility rather than an increase in carrier concentration, which would require slower electrochemical processes. It has been reported that bias can significantly increase the carrier mobility in oxides [75]. Specifically, for ceria-based films, bias has been shown to block ionic conduction due to the segregation of $\text{V}_{\text{O}}^{\bullet}$ at grain boundaries and interfaces while opening parallel paths for electronic conduction [45]. However, this effect has only been

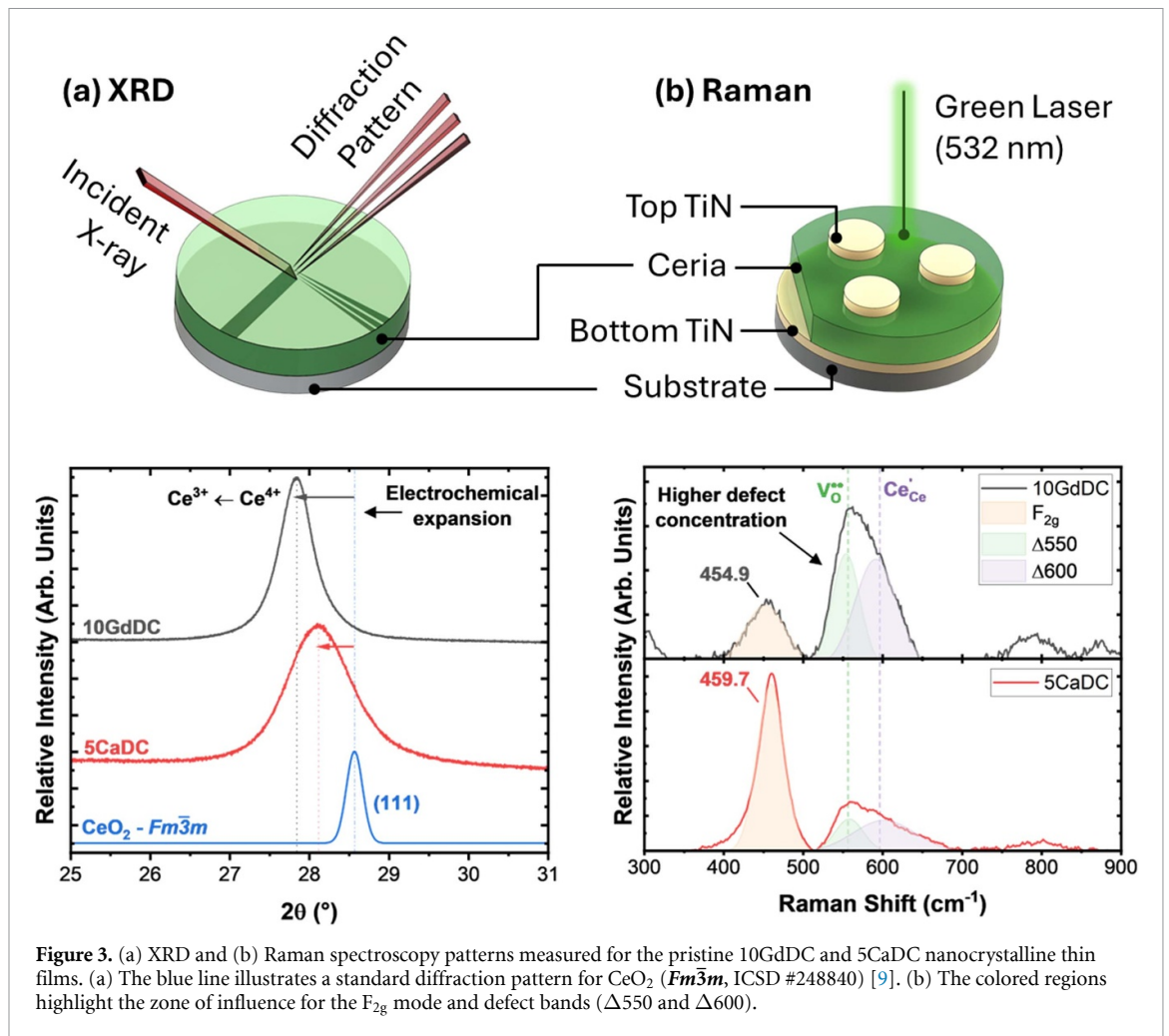


Figure 3. (a) XRD and (b) Raman spectroscopy patterns measured for the pristine 10GdDC and 5CaDC nanocrystalline thin films. (a) The blue line illustrates a standard diffraction pattern for CeO₂ (Fm $\bar{3}$ m, ICSD #248840) [9]. (b) The colored regions highlight the zone of influence for the F_{2g} mode and defect bands (Δ550 and Δ600).

demonstrated for microcrystalline ceramics. Our results for the nanocrystalline ceria films show that bias significantly enhances overall conductivity.

The 5CaDC sample exhibits a response similar to that of 10GdDC, with a sharp increase in ε_r'' under bias. However, unlike 10GdDC, 5CaDC does not return to its original behavior after bias removal, as ε_r'' remains elevated, indicating a non-volatile response likely due to irreversible electrochemical changes. Additionally, the sample shows an increase in ε_r' following bias application, further suggesting that it occurs via polarization mechanisms (figure S12). This observation is consistent with the previously discussed EIS characterization, as seen in figure 2.

When the samples are exposed to high electric fields (bias) for extended periods (\approx hours), the electrical response becomes unstable and exhibits hysteretic behavior. This is particularly evident in figure 4(a), where, after removing the electric field, the sample shows transient behavior that was not present during the bias application. This indicates that a slow process occurred while the bias was active. The electrical characterization also showed hysteresis after a thermal cycle and bias (figures S13 and S15), highlighting the high reactivity of the pristine samples. Therefore, prolonged bias application likely induces electrochemical changes in ceria.

Parallel features become apparent when comparing the dielectric results with the electromechanical response (figures 4(b) and (c)). After prolonged exposure to a bias (3 V) over an extended period (hours), the sample exhibits intrinsic 1st and 2nd harmonic responses. The 2nd harmonic response is expected due to the quadratic coupling between polarization and strain in electrostrictors [4]. The 1st harmonic response is typically linked to piezoelectric behavior [76], although its presence does not necessarily imply piezoelectricity as in dielectrics. Electrostrictors can also show a first-order response when a bias is applied, which ‘linearizes’ the electrostrictive response, often called *pseudo*-piezoelectricity [13, 14]. This effect is observed in figure 4(b), where the bias application enhances the instantaneous 1st harmonic response. However, a weaker first-harmonic response is also observed before bias application, suggesting the presence of a ‘remanent’ built-in bias. This phenomenon has been reported previously [47] and can be induced in thin films due to electrochemical heterogeneity. The built-in response was absent from the pristine samples

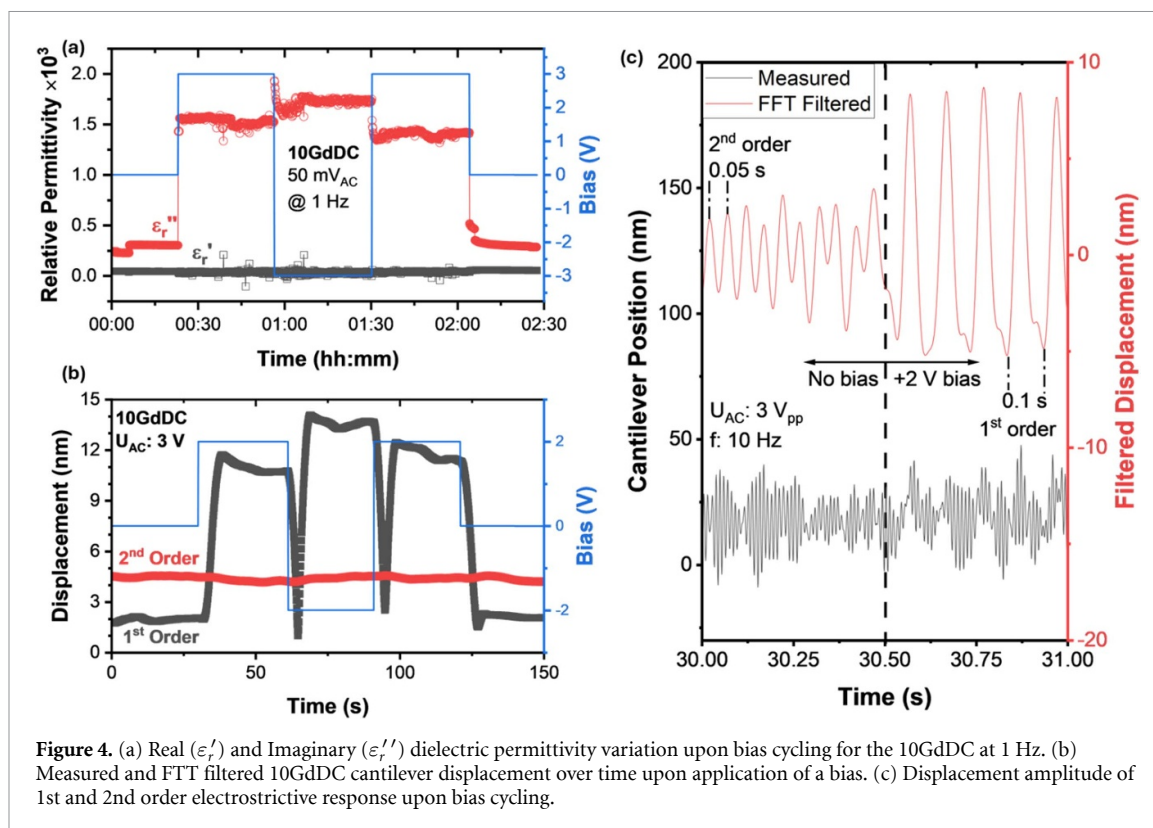


Figure 4. (a) Real (ϵ_r') and Imaginary (ϵ_r'') dielectric permittivity variation upon bias cycling for the 10GdDC at 1 Hz. (b) Measured and FFT filtered 10GdDC cantilever displacement over time upon application of a bias. (c) Displacement amplitude of 1st and 2nd order electrostrictive response upon bias cycling.

(figure S17) and emerged after bias cycling. Previous electrochemical characterization (figure 2) indicated that nanocrystalline films are susceptible to electrochemical changes, leading to the observed built-in first-order electromechanical response.

Additionally, a comparison between ϵ_r'' (figure 4(a)) and cantilever displacement at first and second harmonics (figure 4(c)) reveals further similarities. Both measurements show a small difference in the measured magnitude between positive and negative bias, which is directly attributed to the built-in bias, offsetting the internal polarization depending on the applied field direction. Given the association between polarization, conduction mechanisms, and polaronic features, polarons likely play a role in the observed electromechanical coupling.

3.5. Discussion on polaronic driven electromechanical coupling

Overall, 10GdDC and 5CaDC crystallographic and electrical properties point to a highly defective system dominated by electronic conduction via polaron hopping enabled by the high population of Ce_{Ce}' electronic defects, which are stabilized by the nanostructured films [23].

While Ce_{Ce}' is fundamentally an electronic defect, it forms through the recombination of an electronic charge carrier with a lattice ion residing at the cation site of the fluorite. This defect configuration not only gives rise to the observed polaronic electronic conduction but also couples electrical stimuli to mechanical strain due to the significant ionic radius mismatch between Ce^{3+} and Ce^{4+} . As a result, polaronic transport and defect reconfiguration within the material induce a substantial mechanical response.

The similar defect chemistry configurations in both samples may explain why both films exhibit similar electromechanical performance, regardless of the dopant, as observed in bulk materials [7]. It has been previously reported that enhanced polaronic conductivity can induce a frequency-independent response [77]. Furthermore, when comparing ceria films prepared under different conditions, it was found that nanocrystalline materials exhibit enhanced electromechanical coupling compared to higher crystallinity systems [44].

We find a correlation between polaron-dominated ceria thin films and giant electrostriction, suggesting a dependence on Ce_{Ce}' rather than $\text{V}_{\text{O}}^{\bullet}$. A clear distinction between the contributions of these two types of defects is not trivial, as Ce_{Ce}' is often accompanied by $\text{V}_{\text{O}}^{\bullet}$ to maintain charge balance in the lattice. However, our work aligns with recent studies on non-oxygen defective ceria. Enhanced and frequency-independent electromechanical responses have been observed in polaronic-dominated ceramics, such as Pr-doped ceria, where $\text{Pr}^{4+} - \text{Pr}^{3+}$ pairs are responsible for significant electronic conductivity [77]. Additionally, aliovalent doping, e.g. Zr^{4+} , has been shown to induce extremely high electrostriction ($\sim 10^{-16} \text{ m}^2 \text{ V}^{-2}$) due to the

mobility of Zr^{4+} sites in the lattice under an applied electric field [20]. Interestingly, the presence of oxygen vacancies significantly hampers the electrochemical performance in aliovalent-doped ceria [21].

Therefore, we propose that the large electromechanical coupling in ceria is correlated with dynamic electro-elastic sites rather than oxygen vacancies alone. While oxygen defects do seem to play a role, especially at low frequencies for specific compositions [7, 12, 78], electromechanical coupling may also be influenced by defects on the cation site of ceria, such as Ce_{Ce} or dopant substitution. These cation-site defects do not only create electrostatic and elastic dipoles, but polaronic mechanisms also tend to dominate at low temperatures due to their lower activation energy [61, 79]. While linking giant electrostriction in defective ceria oxides to cationic defects does not automatically explain all observed effects, this new perspective may provide a better understanding and enable tailoring these materials' properties.

4. Conclusions

In conclusion, both 10GdDC and 5CaDC samples exhibit a nanometric morphology due to low-temperature deposition in an oxygen-depleted atmosphere, resulting in a high density of point defects, such as Ce_{Ce} and V_O , as demonstrated by XRD and Raman characterizations. Despite differences in dopant, both samples show a similar electrostrictive response, suggesting that dopant interactions are not the dominant factor in the defect chemistry of these materials. Additionally, both compositions exhibit comparable electrical properties and conductivity, with an activation energy of approximately 0.5 eV. This lower activation energy indicates mixed ionic–electronic conductivity, with a dominant electronic contribution linked to polaron hopping.

A key finding of this work is that the observed electromechanical coupling in ceria-based materials arises not solely from oxygen vacancy migration, as traditionally assumed, but also from defect reorganization at the cation site. The predominance of polaronic mechanisms in both polarization and conduction processes suggests that electronic defects, particularly Ce_{Ce} , may play a critical role in inducing the large electromechanical response. This insight introduces a new perspective in the field, challenging the conventional vacancy-centered models and highlighting the contribution of polaronic conduction to the coupling of electrical and mechanical properties.

By identifying the role of cation-site defects in promoting electromechanical behavior, this study provides a novel framework for understanding defect-driven electromechanical interactions in ceria-based materials. These findings offer new design principles for optimizing functional oxides for applications in energy devices and electromechanical actuators. Furthermore, they align with recent reports on aliovalent doping effects, reinforcing the need to consider multiple defect types beyond oxygen vacancies when developing ceria-based electroactive materials.

Data availability statement

The data that support the findings of this study are openly available at the following URL/DOI: <https://doi.org/10.11583/DTU.27952401>.

Acknowledgment

We acknowledge MAX IV Laboratory for time on Beamline DanMAX under Proposal 20230258. Research conducted at MAX IV, a Swedish national user facility, is supported by Vetenskapsrådet (Swedish Research Council, VR) under Contract 2018-07152, Vinnova (Swedish Governmental Agency for Innovation Systems) under Contract 2018-04969, and Formas under Contract 2019-02496.

This work was funded by the following projects: Micro-mechanical pump for next-generation insulin delivery systems (PRISMA), The European Innovation Council (EIC); Acoustofluidic thin-film actuated chip for exosome separation from blood (ACOUSOME), The European Innovation Council (EIC); VILLUM FONDEN—Research Grant 00022862; Defective metal oxides as the next generation of lead-free piezoelectrics for ultrasonic actuators—DEMETRA, M.ERA-NET, DK-IFD # 118-00006B-98; Horizon Europe Framework Programme (HORIZON-TMA-MSCA-SE), project No. 101131229, Piezoelectricity in 2D-materials: materials, modeling, and applications; European Research Council (ERC) under the European Union's Horizon 2020 research and innovation program (Grant 801847).

Additional funding was provided by the Olle Engkvist Foundation, the Essence project and the Swedish Research Council. We thank the Danish Agency for Science, Technology, and Innovation for funding the instrument center DanScatt (Grant number 2021, 7129-00006B).

Funding

Micro-mechanical pump for next-generation insulin delivery systems (PRISMA), The European Innovation Council (EIC), 101057436 (V E, H B).

Acoustofluidic thin-film actuated chip for exosome separation from blood (ACOUSOME), The European Innovation Council (EIC), 101099787 (V E).

VILLUM FONDEN—Research Grant 00022862 (V E).

Defective metal oxides as the next generation of lead-free piezoelectrics for ultrasonic actuators—DEMETERA, M.ERA-NET, DK-IFD # 118-00006B-98 (V E).

We thank the Danish Agency for Science, Technology, and Innovation for funding the instrument center DanScatt (Grant number 2021, 7129-00006B). (V B T, V E).

Horizon Europe Framework Programme (HORIZON-TMA-MSCA-SE), project No. 101131229, Piezoelectricity in 2D-materials: materials, modeling, and applications (PIEZO 2D). (V E).

This project received funding from the European Research Council (ERC) under the European Union's Horizon 2020 research and innovation program (Grant 801847). Additional funding was provided by the Olle Engkvist Foundation, the Essence project and the Swedish Research Council. (J W).

Author contributions

Conceptualization: V E, V B T.

Methodology: V B T, H C, I K, V F, H B.

Investigation: V B T, M V, H C, V F, M G, H B, V E, J W.

Visualization: V B T, H C, M G, H C, V E.

Funding acquisition: V E.

Project administration: V E.

Supervision: V E, J W, H B.

Writing—original draft: V B T.

Writing—review and editing: V B T, V E, H B.

Conflict of interest

The authors declare no conflict of interest.

ORCID iDs

Victor Buratto Tinti  <https://orcid.org/0000-0001-5759-0214>

Milica Vasiljevic  <https://orcid.org/0000-0003-0629-8760>

Mathias Grønberg  <https://orcid.org/0009-0003-0624-5762>

Huaiyu Chen  <https://orcid.org/0000-0002-5122-486X>

Valdemar Frederiksen  <https://orcid.org/0000-0001-9390-7055>

Innokenty Kantor  <https://orcid.org/0000-0001-5132-8354>

Jesper Wallentin  <https://orcid.org/0000-0001-5909-0483>

Henrik Bruus  <https://orcid.org/0000-0001-5827-2939>

Vincenzo Esposito  <https://orcid.org/0000-0002-9817-7810>

References

- [1] Sundar V and Newnham R E 1992 Electrostriction and polarization *Ferroelectrics* **135** 431–46
- [2] Cross L E, Jang S J, Newnham R E, Nomura S and Uchino K 1980 Large electrostrictive effects in relaxor ferroelectrics *Ferroelectrics* **23** 187–91
- [3] Newnham R E, Sundar V, Yimnirun R, Su J and Zhang Q M 1997 Electrostriction: nonlinear electromechanical coupling in solid dielectrics *J. Phys. Chem. B* **101** 10141–50
- [4] Yu J and Janolin P-E 2022 Defining “giant” electrostriction *J. Appl. Phys.* **131** 170701
- [5] Korobko R, Patlolla A, Kossov A, Wachtel E, Tuller H L, Frenkel A I and Lubomirsky I 2012 Giant electrostriction in Gd-doped ceria *Adv. Mater.* **24** 5857–61
- [6] Schmitt R, Nenning A, Kraynis O, Korobko R, Frenkel A I, Lubomirsky I, Haile S M and Rupp J L M 2020 A review of defect structure and chemistry in ceria and its solid solutions *Chem. Soc. Rev.* **49** 554–92
- [7] Tinti V B, Kabir A, de Florio D Z and Esposito V 2024 Electromechanical coupling in alkaline-earth doped-ceria ceramics *Acta Mater.* **281** 120361
- [8] Wachtel E and Lubomirsky I 2011 The elastic modulus of pure and doped ceria *Scr. Mater.* **65** 112–7
- [9] Artini C, Pani M, Carnasciali M M, Plaisier J R and Costa G A 2016 Lu-, Sm-, and Gd-doped ceria: a comparative approach to their structural properties *Inorg. Chem.* **55** 10567–79

- [10] Kabir A, Tinti V B, Santucci S, Varenik M, Griffiths S, Molin S, Lubomirsky I and Esposito V 2024 Non-classical electrostriction in calcium-doped cerium oxide ceramics *J. Mater. Chem. A* **12** 9173–83
- [11] Varenik M, Nino J C, Wachtel E, Kim S, Cohen S R and Lubomirsky I 2021 Trivalent dopant size influences electrostrictive strain in ceria solid solutions *ACS Appl. Mater. Interfaces* **13** 20269–76
- [12] Varenik M, Nino J C, Wachtel E, Kim S, Yehekel O, Yavo N and Lubomirsky I 2020 Dopant concentration controls quasi-static electrostrictive strain response of ceria ceramics *ACS Appl. Mater. Interfaces* **12** 39381–7
- [13] Korobko R, Wachtel E and Lubomirsky I 2013 Cantilever resonator based on the electrostriction effect in Gd-doped ceria *Sens. Actuators A* **201** 73–78
- [14] Tinti V B et al 2024 Oxygen defective electrostrictors for soft electromechanics *Sci. Adv.* **10** eadq3444
- [15] Tinti V B, Kabir A, de Florio D Z and Esposito V 2023 The role of dopant on the defect chemistry of metal oxides *Metal Oxide Defects* (Elsevier) pp 313–53
- [16] Korobko R, Lerner A, Li Y, Wachtel E, Frenkel A I and Lubomirsky I 2015 In-situ extended x-ray absorption fine structure study of electrostriction in Gd doped ceria *Appl. Phys. Lett.* **106** 042904
- [17] Santucci S, Zhang H, Sanna S, Pryds N and Esposito V 2020 Electro-chemo-mechanical effect in Gd-doped ceria thin films with a controlled orientation *J. Mater. Chem. A* **8** 14023–30
- [18] Santucci S, Zhang H, Kabir A, Marini C, Sanna S, Han J K, Ulbrich G, Heppke E M, Castelli I E and Esposito V 2021 Electromechanically active pair dynamics in a Gd-doped ceria single crystal *Phys. Chem. Chem. Phys.* **23** 11233–9
- [19] Das T, Nicholas J D, Sheldon B W and Qi Y 2018 Anisotropic chemical strain in cubic ceria due to oxygen-vacancy-induced elastic dipoles *Phys. Chem. Chem. Phys.* **20** 15293–9
- [20] Varenik M et al 2023 Lead-free Zr-doped ceria ceramics with low permittivity displaying giant electrostriction *Nat. Commun.* **14** 7371
- [21] Pechersky-Savich T et al 2024 Correlated displacement of dynamic elastic dipoles produces nonclassical electrostriction in Zr-doped ceria *Chem. Mater.* **36** 7665–75
- [22] Santucci S et al 2025 Enhanced non-classical electrostriction in strained tetragonal ceria *Nat. Commun.* **16** 36
- [23] Tuller H L and Nowick A S 1977 Small polaron electron transport in reduced CeO₂ single crystals *J. Phys. Chem. Solids* **38** 859–67
- [24] Navarro L, Marques F and Frade J 1997 n-type conductivity in gadolinia-doped ceria *J. Electrochem. Soc.* **144** 267–73
- [25] Ni D W, de Florio D Z, Marani D, Kaiser A, Tinti V B and Esposito V 2015 Effect of chemical redox on Gd-doped ceria mass diffusion *J. Mater. Chem. A* **3** 18835–8
- [26] Shannon R D 1976 Revised effective ionic radii and systematic studies of interatomic distances in halides and chalcogenides *Acta Crystallogr. A* **32** 751–67
- [27] Wachtel E, Frenkel A I and Lubomirsky I 2018 Anelastic and electromechanical properties of doped and reduced ceria *Adv. Mater.* **30** 1–17
- [28] Santucci S, Zhang H, Sanna S, Pryds N and Esposito V 2019 Enhanced electro-mechanical coupling of TiN/Ce_{0.8}Gd_{0.2}O_{1.9} thin film electrostrictor *APL Mater.* **7** 071104
- [29] Jørgensen M R V, Sørensen D R, Kantor I and Oller S F 2021 DanMAX—the new materials science beamline at MAX IV *Acta Crystallogr. A* **77** C821
- [30] Tinti V B 2025 Supporting dataset for the publication “Electromechanical coupling in polaronic ceria” Dataset Technical University of Denmark (<https://doi.org/10.11583/DTU.27952401.v1>)
- [31] Steckel A G, Bruus H, Muralt P and Matloub R 2021 Fabrication, characterization, and simulation of glass devices with AlN thin-film transducers for excitation of ultrasound resonances *Phys. Rev. Appl.* **16** 014014
- [32] Steckel A G and Bruus H 2021 Numerical study of bulk acoustofluidic devices driven by thin-film transducers and whole-system resonance modes *J. Acoust. Soc. Am.* **150** 634–45
- [33] Landau L D and Lifshitz E M 1984 Electrodynamics of continuous media *Course of Theoretical Physics* 2nd edn, vol 8 (Pergamon) (<https://doi.org/10.1016/B978-0-08-030275-1.50025-4>)
- [34] Badwal S P S, Fini D, Ciacchi F T, Munnings C, Kimpton J A and Drennan J 2013 Structural and microstructural stability of ceria—gadolinia electrolyte exposed to reducing environments of high temperature fuel cells *J. Mater. Chem. A* **1** 10768
- [35] Yavo N, Noiman D, Wachtel E, Kim S, Feldman Y, Lubomirsky I and Yehekel O 2016 Elastic moduli of pure and gadolinium doped ceria revisited: sound velocity measurements *Scr. Mater.* **123** 86–89
- [36] Blumenthal R N, Brugner F S and Garnier J E 1973 The electrical conductivity of CaO-doped nonstoichiometric cerium dioxide from 700° to 1500 °C *J. Electrochem. Soc.* **120** 1230
- [37] Souza E C C, Chueh W C, Jung W, Muccillo E N S and Haile S M 2012 Ionic and electronic conductivity of nanostructured, samaria-doped ceria *J. Electrochem. Soc.* **159** K127–K35
- [38] Pandey A K and Pratap R 2007 Effect of flexural modes on squeeze film damping in MEMS cantilever resonators *J. Micromech. Microeng.* **17** 2475–84
- [39] Kabir A, Zhang H, Colding-Jørgensen S, Santucci S, Molin S and Esposito V 2020 Electro-chemo-mechanical properties in nanostructured Ca-doped ceria (CDC) by field assisted sintering *Scr. Mater.* **187** 183–7
- [40] Yavo N, Yehekel O, Wachtel E, Ehre D, Frenkel A I and Lubomirsky I 2018 Relaxation and saturation of electrostriction in 10 mol% Gd-doped ceria ceramics *Acta Mater.* **144** 411–8
- [41] Kabir A, Buratto Tinti V, Varenik M, Lubomirsky I and Esposito V 2020 Electromechanical dopant–defect interaction in acceptor-doped ceria *Mater. Adv.* **1** 2717–20
- [42] Meessen K J, Paulides J J H and Lomonova E A 2013 Force calculations in 3-D cylindrical structures using Fourier analysis and the Maxwell stress tensor *IEEE Trans. Magn.* **49** 536–45
- [43] Park G-T, Choi J-J, Ryu J, Fan H and Kim H-E 2002 Measurement of piezoelectric coefficients of lead zirconate titanate thin films by strain-monitoring pneumatic loading method *Appl. Phys. Lett.* **80** 4606–8
- [44] Hadad M, Ashraf H, Mohanty G, Sandu C and Muralt P 2016 Key-features in processing and microstructure for achieving giant electrostriction in gadolinium doped ceria thin films *Acta Mater.* **118** 1–7
- [45] Sulekar S S, Ordóñez J E, Arango I C, Gomez M E and Nino J C 2019 Effect of a DC bias on the conductivity of gadolinia doped ceria thin films *Electrochim. Acta* **303** 275–83
- [46] Mishuk E, Ushakov A, Makagon E, Cohen S R, Wachtel E, Paul T, Tsur Y, Shur V Y, Kholkin A and Lubomirsky I 2019 Electro-chemomechanical contribution to mechanical actuation in Gd-doped ceria membranes *Adv. Mater. Interfaces* **6** 1801592
- [47] Mishuk E, Ushakov A D, Cohen S R, Shur V Y, Kholkin A L and Lubomirsky I 2018 Built-in bias in Gd-doped ceria films and its implication for electromechanical actuation devices *Solid State Ion.* **327** 47–51

- [48] Kraynis O, Makagon E, Mishuk E, Hartstein M, Wachtel E, Lubomirsky I and Livneh T 2019 Suitability of Raman spectroscopy for assessing anisotropic strain in thin films of doped ceria *Adv. Funct. Mater.* **29** 1804433
- [49] Tsuchiya M, Bojarczuk N A, Guha S and Ramanathan S 2009 Microstructural effects on electrical conductivity relaxation in nanoscale ceria thin films *J. Chem. Phys.* **130** 174711
- [50] Sediva E, Bohdanov D, Harrington G F, Rafalovskyi I, Drahokoupil J, Borodavka F, Marton P and Hlinka J 2020 Anisotropic strain in rare-earth substituted ceria thin films probed by polarized Raman spectroscopy and first-principles calculations *ACS Appl. Mater. Interfaces* **12** 56251–9
- [51] Chaikasetsin S et al 2021 Thermal expansion characterization of thin films using harmonic Joule heating combined with atomic force microscopy *Appl. Phys. Lett.* **118** 194101
- [52] Arndt B, Noei H, Keller T F, Müller P, Vonk V, Nanning A, Opitz A K, Fleig J, Rütt U and Stierle A 2016 Structure and stability of Gd-doped CeO₂ thin films on yttria-stabilized zirconia *Thin Solid Films* **603** 56–61
- [53] Marrocchelli D, Bishop S R, Tuller H L and Yildiz B 2012 Understanding chemical expansion in non-stoichiometric oxides: ceria and zirconia case studies *Adv. Funct. Mater.* **22** 1958–65
- [54] Graham J T, Zhang Y and Weber W J 2018 Irradiation-induced defect formation and damage accumulation in single crystal CeO₂ *J. Nucl. Mater.* **498** 400–8
- [55] Takaki S, Yasuda K, Yamamoto T, Matsumura S and Ishikawa N 2014 Atomic structure of ion tracks in ceria *Nucl. Instrum. Methods Phys. Res. B* **326** 140–4
- [56] Kim S and Maier J 2002 On the conductivity mechanism of nanocrystalline ceria *J. Electrochem. Soc.* **149** J73
- [57] Wang S, Kobayashi T, Dokiya M and Hashimoto T 2000 Electrical and ionic conductivity of Gd-doped ceria *J. Electrochem. Soc.* **147** 3606
- [58] Chiang Y-M, Lavik E B, Kosacki I, Tuller H L and Ying J Y 1996 Defect and transport properties of nanocrystalline CeO_{2-x} *Appl. Phys. Lett.* **69** 185–7
- [59] RUPP J and Gauckler L 2006 Microstructures and electrical conductivity of nanocrystalline ceria-based thin films *Solid State Ion.* **177** 2513–8
- [60] Tschöpe A, Ying J Y and Tuller H L 1996 Catalytic redox activity and electrical conductivity of nanocrystalline non-stoichiometric cerium oxide *Sens. Actuators B* **31** 111–4
- [61] Tschöpe A and Birringer R 2001 Grain size dependence of electrical conductivity in polycrystalline cerium oxide *J. Electroceram.* **7** 169–77
- [62] Samet M, Levchenko V, Boiteux G, Seytre G, Kallel A and Serghei A 2015 Electrode polarization vs. Maxwell-Wagner-Sillars interfacial polarization in dielectric spectra of materials: characteristic frequencies and scaling laws *J. Chem. Phys.* **142** 194703
- [63] Kalaev D, Defferriere T, Nicollet C, Kadosh T and Tuller H L 2020 Dynamic current–voltage analysis of oxygen vacancy mobility in praseodymium-doped ceria over wide temperature limits *Adv. Funct. Mater.* **30** 1907402
- [64] Tuller H 2000 Ionic conduction in nanocrystalline materials *Solid State Ion.* **131** 143–57
- [65] Sun L, Hao X, Meng Q, Wang L, Liu F and Zhou M 2019 Polaronic resistive switching in ceria-based memory devices *Adv. Electron. Mater.* **5** 1900271
- [66] Khera E A, Ullah H, Hussain F, Imran M, Khalil R M A, Sattar M A, Rana A M, Mahata C and Kim S 2020 Investigation of structural and electronic properties of doped ceria Ce_{1-x}M_xO₂ (M=Hf,Ti,Ba,Mg,Nb,Vx=0.25%) for ReRAM applications: a first principles study *Physica E* **119** 114025
- [67] Scherrer P 1918 Bestimmung der Größe und der inneren Struktur von Kolloidteilchen mittels Röntgenstrahlen, Nachrichten von Der Gesellschaft Der Wissenschaften Zu Göttingen *Math. Klasse* **1918** 98–100 (available at: <http://eudml.org/doc/59018>)
- [68] Monshi A, Foroughi M R and Monshi M R 2012 Modified Scherrer equation to estimate more accurately nano-crystallite size using XRD *World J. Nano Sci. Eng.* **02** 154–60
- [69] Mishuk E, Makagon E, Wachtel E, Cohen S R, Popovitz-Biro R and Lubomirsky I 2017 Self-supported Gd-doped ceria films for electromechanical actuation: fabrication and testing *Sens. Actuators A* **264** 333–40
- [70] Kim D-J and Parameters L 1989 Ionic conductivities, and solubility limits in fluorite-structure MO₂ oxide [M = Hf⁴⁺, Zr⁴⁺, Ce⁴⁺, Th⁴⁺, U⁴⁺] solid solutions *J. Am. Ceram. Soc.* **72** 1415–21
- [71] Kossov A, Feldman Y, Wachtel E, Gartsman K, Lubomirsky I, Fleig J and Maier J 2006 On the origin of the lattice constant anomaly in nanocrystalline ceria *Phys. Chem. Chem. Phys.* **8** 1111
- [72] Deshpande S, Patil S, Kuchibhatla S V and Seal S 2005 Size dependency variation in lattice parameter and valency states in nanocrystalline cerium oxide *Appl. Phys. Lett.* **87** 133113
- [73] Weber W H, Hass K C and McBride J R 1993 Raman study of CeO₂: second-order scattering, lattice dynamics, and particle-size effects *Phys. Rev. B* **48** 178–85
- [74] Nakajima A, Yoshihara A and Ishigame M 1994 Defect-induced Raman spectra in doped CeO₂ *Phys. Rev. B* **50** 13297–307
- [75] Kemp D, De Souza R A and Stone O 2024 Two birds: using high electric fields to enhance the mobility and the concentration of point defects in ion-conducting solids *J. Am. Ceram. Soc.* **146** 4783–94
- [76] Park D-S et al 2022 Induced giant piezoelectricity in centrosymmetric oxides *Science* **375** 653–7
- [77] Tinti V B, Kabir A, Han J K, Molin S and Esposito V 2021 Gigantic electro-chemo-mechanical properties of nanostructured praseodymium doped ceria *Nanoscale* **13** 7583–9
- [78] Kabir A, Santucci S, Van Nong N, Varenik M, Lubomirsky I, Nigon R, Murali P and Esposito V 2019 Effect of oxygen defects blocking barriers on gadolinium doped ceria (GDC) electro-chemo-mechanical properties *Acta Mater.* **174** 53–60
- [79] Suzuki T, Kosacki I, Anderson H U and Colomban P 2001 Electrical conductivity and lattice defects in nanocrystalline cerium oxide thin films *J. Am. Ceram. Soc.* **84** 2007–14